ACS OMEGA

http://pubs.acs.org/journal/acsodf

Article

Additive Manufacturing of Viscoelastic Polyacrylamide Substrates for Mechanosensing Studies

Fardeen Kabir Protick, Sadat Kamal Amit, Kshitij Amar, Shukantu Dev Nath, Rafee Akand, Virginia A. Davis,* Sabrina Nilufar,* and Farhan Chowdhury*

Cite This: *ACS Omega* 2022, 7, 24384−24395

Read Online

ACCESS | Metrics & More | Article Recommendations | Supporting Information

ABSTRACT: Polymerized polyacrylamide (PAA) substrates are linearly elastic hydrogels that are widely used in mechanosensing studies due to their biocompatibility, wide range of functionalization capability, and tunable mechanical properties. However, such cellular response on purely elastic substrates, which do not mimic the viscoelastic living tissues, may not be physiologically relevant. Because the cellular response on 2D viscoelastic PAA substrates remains largely unknown, we used stereolithography (SLA)-based additive manufacturing technique to create viscoelastic PAA substrates with tunable mechanical properties that allow us to identify physiologically relevant cellular behaviors. Three PAA substrates of different complex moduli were fabricated by SLA. By embedding fluorescent markers during the additive manufacturing of the substrates, we show a homogeneous and uniform composition throughout, which conventional manufacturing techniques cannot produce. Rheological investigation of the additively manufactured PAA substrates shows a viscoelastic behavior with a 5−10% loss moduli compared to their elastic moduli, mimicking the living tissues. To understand the cell mechanosensing on the dissipative PAA substrates, single live cells were seeded on PAA substrates to establish the basic relationships between cell traction, cytoskeletal prestress, and cell spreading. With the increasing substrate moduli, we observed a concomitant increase in cellular traction and prestress, but not cell spreading, suggesting that cell spreading can be decoupled from traction and intracellular prestress in physiologically relevant environments. Together, additively manufactured PAA substrates fill the void of lacking real tissue like viscoelastic materials that can be used in a variety of mechanosensing studies with superior reproducibility.

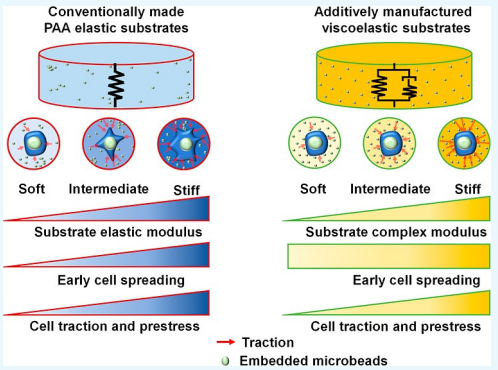

1. INTRODUCTION

The cytoskeletal prestress is a master regulator of critical cellular functions.[1] In the last two decades, many mechanosensing studies show that cytoskeletal prestress regulates cell spreading,[2] migration,[3] chemotaxis,[4] cell fate determination,[5−7] immune cell activation,[8] malignancy and cancer progression,[9] and dictates many other fundamental cell behaviors including, but not limited to, rigidity sensing,[10] cellular adaptation to microenvironment stiffness,[11] and nuclear mechanotransduction.[12−14] A majority of these studies relied on flexible polyacrylamide (PAA) substrates for regulating cytoskeletal prestress. The crosslinked PAA substrates are nontoxic, biocompatible, hydrophilic, and offer a wide range of functionalization capabilities. In addition, the tunability of mechanical stiffness of the flexible substrates is a very attractive feature of PAA substrates. Collectively, the flexible PAA substrates are at the heart of mechanotransduction and mechanosensing studies. However, the fabrication of PAA substrates is technically challenging, thus dependent on the user expertise level, restricted to specific shapes, tedious and time-consuming, not suitable for high-throughput production, and does not allow good control over local polymerization reactions. As a result, there could be local property variations and batch−batch reproducibility issues which may lead to confounding results.

With the advent of additive manufacturing, many of the shortcomings of PAA substrate fabrication by conventional processes could be avoided altogether. Among the additive manufacturing technologies, vat polymerization, also known as the stereolithography (SLA) technique, is best suited for PAA substrate manufacturing. SLA is a process where liquid photoactivatable resin is cured by a UV light source. SLA is faster, cheaper, efficient, and highly customizable in terms of shape and thickness.[15] Additionally, the SLA technique eliminates user expertise dependence during fabrication, reduces the batch−batch variation, and most importantly provides greater control of local properties. Here, we utilized

Received: March 24, 2022
Accepted: June 23, 2022
Published: July 6, 2022

https://doi.org/10.1021/acsomega.2c01817
ACS Omega 2022, 7, 24384−24395

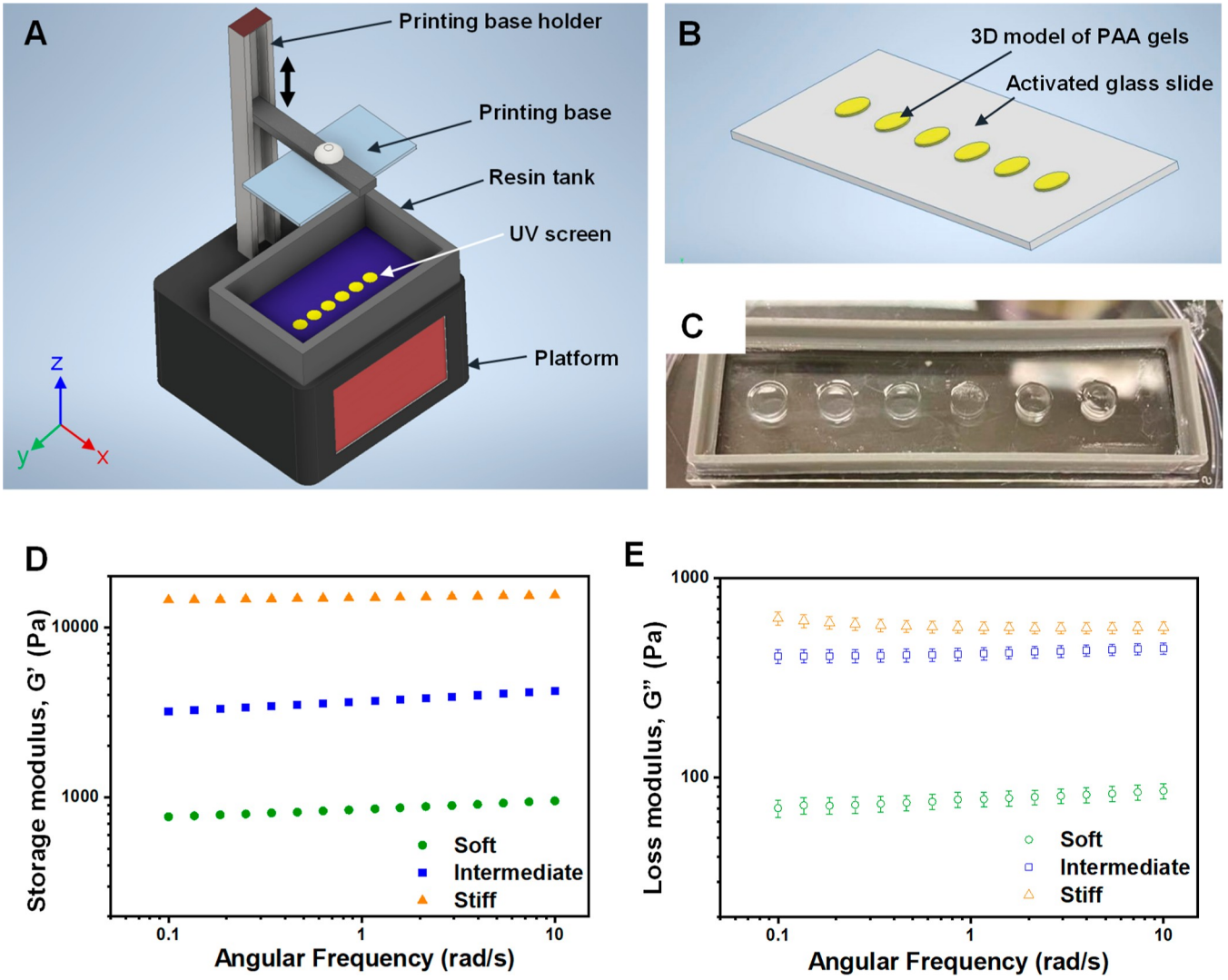

Figure 1. Additive manufacturing of viscoelastic PAA substrates. (A) Schematic of an SLA 3D printer showing major components. A representative circular design of the substrate array is displayed in the resin tank where the light source emits UV light for photopolymerization. (B) 3D model of an array of substrates is used for printing. The substrates can be printed in any desired shape and thickness as low as 50 μm. Here, a circular substrate array (yellow) is shown on an activated glass slide. (C) Additively manufactured PAA substrates on an activated glass slide. As shown in the 3D model, six gels were printed on the activated glass slide. A reusable confinement boundary (gray) is affixed on the slide for subsequent cleaning, functionalization, and experimentation. (D,E) Additively manufactured PAA substrates show tunable viscoelastic properties. Soft (green), intermediate (blue), and stiff (orange) substrates show 5−10% viscous dissipation capacity compared to their respective elastic modulus. Data represent mean ± s.e. and are from 3 independent experiments.

the SLA technique to manufacture PAA substrates with three different monomer to crosslinker ratios, namely, 10% acrylamide: 0.15% bis-acrylamide, 10% acrylamide: 0.30% bis-acrylamide, and 10% acrylamide: 1.2% bis-acrylamide, to investigate the mechanical and rheological properties, porosity, surface topography, homogeneity, and suitability for mechanosensing studies such as traction force microscopy (TFM) on varying substrate stiffness. Our optimized SLA technique to manufacture PAA substrates can be used to interrogate many single-cell behaviors with all the benefits that come along with additive manufacturing.

2. MATERIALS AND METHODS

2.1. Additive Manufacturing and Functionalization of PAA Substrates. We used vat photopolymerization, also known as SLA, with a 405 nm UV light source to print PAA substrates. The photoreactive resin mixture was placed in the resin tank while the UV light source focuses on the $x-y$ plane (Figure 1). The printing base containing the glass slide was lowered into the tank and moved in the z-direction (Figure 1). Our SLA 3D printer used a bottom-up approach, where the source UV light, placed under the resin tank, shone in the upward direction. The gap between the printing base and resin tank determined each layer's height. As the UV light cured the photoreactive resin, the printing base was raised incrementally by an amount set by each layer thickness. This bottom-up approach is precise and provides greater control over the printing process.[15] The SLA 3D printer allows design flexibility (e.g., shape, size, and thickness) for the additive manufacturing of PAA substrates.

During the initial runs, we identified some key factors and parameters that regulate the properties of additively manufactured PAA substrates. Source ultraviolet wavelength, time of exposure, choice of photoinitiators and their concentrations,

https://doi.org/10.1021/acsomega.2c01817
ACS Omega 2022, 7, 24384−24395

substrate thickness, resting time after printing, and monomer to crosslinker concentration were some of the key factors and parameters that could potentially affect the fabrication process. Some of the key factors were fixed (due to the inherent specifications of the SLA 3D printer) leading to the choice of additional dependent factors, while the others could be varied. For example, the source UV wavelength was fixed at 405 nm. Therefore, we were limited to choosing photoinitiators corresponding to 405 nm. The photoinitiator Irgacure 2959 (I2959) could not be used despite being the most widely used photoinitiator in the market.[16] To photoactivate the acrylamide: bis-acrylamide mixtures, we carefully evaluated several photoinitiators, namely, TPO, TPO-Li, and PEG-BAPO which are known to be photoreactive around 405 nm.[17−19] Performances of these photoinitiators along with a relative comparison are shown in Table 1. In our studies, TPO-Li was best suited due to the high absorption coefficient around 405 nm. Besides, TPO-Li was biocompatible and very affordable.[20]

Table 1. Comparison of Various Photoinitiators for Additive Manufacturing of PAA Substrates

properties	TPO	TPO-Li	BAPO
activation wavelength	385−420 nm	360−410 nm	390−430 nm
solubility	water soluble	water soluble	acetone soluble
printing quality	stable, well-defined boundaries	stable, polymerizes readily	stable, 70% gels polymerized
time of exposure	20 s	30 s	45 s
concentration	2.4% v/v	2.0% v/v	3.0% v/v

By using an additive manufacturing technique for PAA substrates, we benefitted from the freedom and flexibility in designing different shapes and sizes of the gels as needed. The hydrogels were designed and printed with varying sizes and thicknesses depending on the application and characterization technique. For single living-cell applications, we designed and printed circular gels of 25 mm diameter and height ranging between 50 and 250 μm on a glass slide. The z-axis resolution of the printer was limited to 50 μm, so the printed samples had to be in multiples of 50 μm. For scanning electron microscopy (SEM) studies, we printed circular substrates of 25 mm diameter and 1 mm height. For atomic force microscope (AFM) studies, we prepared 16 mm diameter and 2 mm height substrates. For bulk rheological measurements, we printed circular gels of 30 mm diameter and 1 mm height.

We followed the previously described glass surface preparation for PAA substrate attachment and made some modifications as described below.[21,22] First, 3-aminopropylmethoxysilane (97%, Sigma-Aldrich) was smeared over the glass surfaces and left for 15 min. The slides were placed inside a solution containing 0.5% silane in ddH_2O for 10 min while stirring. Silanized slides were taken out and rinsed for 10 min in ddH_2O while stirring. The slides were placed inside an oven for 1 h at 160 °C. The dried slides were placed in the desiccator for 15 min to cool off. The slides were immersed in 0.5% glutaraldehyde (Grade II, Sigma-Aldrich) for 30 min. Activated glass slides were washed 2×, 6 min each time, with ddH_2O to rinse off excess glutaraldehyde.

Acrylamide solution was prepared by mixing different proportions of 40% acrylamide solution (Bio-Rad) and 2% bis solution (Bio-Rad) with water. 0.4% fluorosphere carboxylate microbeads (0.2 μm, yellow-green color, Life Technologies) were added to the solution. 2% v/v lithium phenyl-2,4,6-trimethylbenzoylphosphinate (Colorado Photopolymer Solutions, Sartumer, Arkema) photoinitiator was added to activate the solution under UV light. Because the photoinitiator was sensitive to light, the solution was kept wrapped in aluminum foil from that point onward.

A prepared glass slide, as described above, was mounted upside down on the printing base so that the activated surface was facing the UV light source. Acrylamide solution was poured into the vat/resin tank of the SLA 3D printer (Monoprice) and the printing process was initiated. A previously designed substrate array was selected for printing and the exposure time was 30 s/layer. After the PAA substrates were printed on the glass slide, they were submerged in phosphate-buffered saline or PBS (1×) for 15 min to rinse off any excess acrylamide solution. The printed PAA substrates were kept in 100 mM HEPES solution.

To functionalize the top surface of the PAA substrates, 100 μM TFPA-PEG_3-Biotin (Thermo Fisher Scientific) was added to the gel surface. The PAA substrates were placed under UV light for activation for 5 min on an ice pack. To ensure uniform surface coverage, the process was repeated twice and washed with PBS in-between steps. Next, 200 μg/mL of NeutrAvidin (Thermo Fisher Scientific) was added to the PAA substrates for 10 min. The NeutrAvidin solution was removed, and the PAA substrates were washed with PBS. RGD-Biotin (Peptides International; concentration of 10 μM) was added to the PAA substrate and incubated for 1 h. Next, the PAA substrates were washed with PBS and were ready for cell plating.

2.2. Conventional Manufacturing of PAA Substrates. PAA gel substrates were prepared as described elsewhere.[22−24] The PAA substrates with 10% acrylamide and 0.15% bis-acrylamide were fabricated. Fluorosphere carboxylate microbeads (0.2 μm, Life Technologies) with yellow-green color were added to the solution mix before setting up the polymerization reactions initiated by ammonium persulfate and tetramethylethylenediamine.

2.3. Routine Cell Culture and Cell Experiments. B16F1 mouse melanoma cell line was routinely cultured on 2D 6-well dishes with a high-glucose DMEM (Invitrogen) medium that contains 10% fetal bovine serum (Gibco) at 37 °C with 5% CO_2. The cell culture medium was also supplemented with 2 mM L-glutamine (Thermo Fisher Scientific), 1 mM sodium pyruvate (Thermo Fisher Scientific), and 50 μg/mL penicillin−streptomycin (Thermo Fisher Scientific). Cells were cultured to 90% confluency before seeding on 2D PAA substrates for TFM. Before seeding the cells, the slides were taken out from 4 °C and kept in RT in order to avoid cold shock. The cells were dislodged using 0.25% Trypsin−EDTA and were seeded on the additively manufactured PAA substrates with DPBS (Thermo Fisher Scientific) containing calcium and magnesium for 4 h before TFM experiments.

2.4. Rheological Measurements. Small amplitude oscillatory shear (SAOS) rheology was used to evaluate the impact of monomer and crosslinker composition on the viscoelastic properties of SLA-printed PAA substrates. An Anton Paar (Ashland, VA) MCR301 rotational rheometer was used to determine the effects of composition on viscoelastic properties at 25 °C. For each composition, disks were printed using SLA and stored in PBS. The substrates were tested using parallel plates at gaps between 0.9 and 1.0 mm; the samples

https://doi.org/10.1021/acsomega.2c01817
ACS Omega 2022, 7, 24384−24395

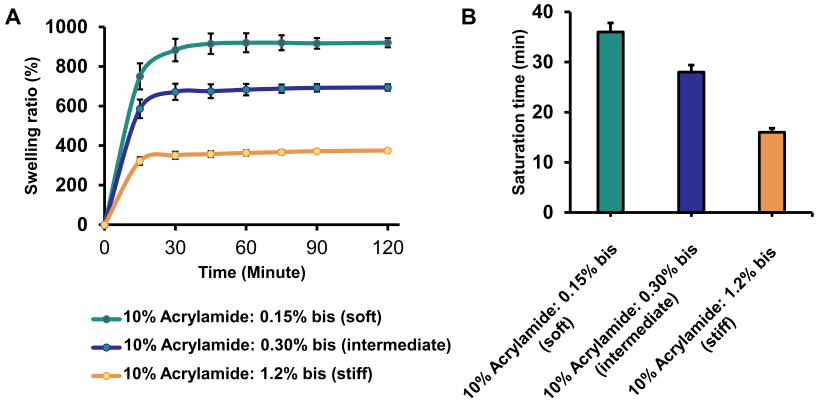

Figure 2. Increasing the stiffness reduces the physical swelling and fluid retention capability of PAA hydrogels. (A) Swelling ratio estimation of three different concentrations (10% acrylamide: 0.15% bis-acrylamide, 10% acrylamide: 0.3% bis-acrylamide, and 10% acrylamide: 1.2% bis-acrylamide) of gels is presented here. The lowest bis-acrylamide concentration was labeled as soft gels while intermediate and high bis-acrylamide concentrations were labeled as intermediate and stiff gels, respectively. Soft gels (green line) show the highest swelling compared to intermediate (blue line) and stiff (orange line) gels. n = 10 for each gel from 3 independent experiments. Data represents mean ± s.e. (B) Saturation time of three different substrates is shown here. The soft gels require the highest time to reach saturation while the stiff gels require the least time to reach saturation. n = 10 for each gel from 3 independent experiments. Data represents mean ± s.e.

were trimmed after lowering the top plate. To prevent evaporation, an evaporation blocker was used, and PBS was placed around the sample. The upper limit of the linear viscoelastic region (LVR) for each sample was based on a 5% decrease in the storage modulus G' during an amplitude (strain) sweep at frequency w = 2 rad/s. Viscoelastic properties were then measured at a strain within the LVR for frequencies ranging from 0.1 to 10 rad/s. After testing, it was visually confirmed that the sample remained intact.

2.5. Measurements of Traction Stress and Cellular Prestress. To understand the interactions between cells and viscoelastic PAA substrates, we employed TFM analysis.[25] TFM studies were conducted on an inverted Leica DMi8 epifluorescence microscope equipped with an ORCA Flash 4.0 V2 sCMOS camera. As the cells adhered and spread on the substrates, the resultant substrate deformation field was quantified by fluorescent microbeads embedded within the substrates. The displacement field and the elastic modulus of the PAA substrates allow us to calculate the traction stress field using the Boussinesq solution in Fourier space as explained elsewhere.[25] Elastic moduli of the substrate stiffness were computed from the shear modulus of the substrates assuming a Poisson's ratio of 0.49 for PAA substrates using constitutive relations.

2.6. Image Analysis. Pore size/ area quantification was carried out by ImageJ software. SEM images were opened in ImageJ software and set to scale. Freehand or polygon selection tool allowed for measuring the area, boundary thickness, and perimeter of each pore. The circularity index or cell shape index (CSI) of each pore was computed using the formula ($\mathrm{CSI} = \frac{4 \bullet \pi \bullet \mathrm{Area}}{\mathrm{Perimeter}^2}$). For the perfect circle, CSI will be 1.0. A lower CSI value for each pore indicates a deviation from the perfect circle.

2.7. Statistical Analysis. Statistical analyses were performed using either a two-tailed Student's t-test or one-way ANOVA.

3. RESULTS

3.1. Additive Manufacturing of PAA Substrates with Tunable Viscoelastic Properties. We used an SLA 3D printer, with a 405 nm UV light source to print PAA substrates (Figure 1A). The SLA 3D printer allows design flexibility (e.g., shape, size, and thickness) for the additive manufacturing of PAA substrates. We designed our PAA hydrogels with varying sizes and thicknesses depending on the application and characterization techniques (Figure 1B,C). For demonstration purposes, here we show six circular PAA hydrogels printed on activated glass slides (Figure 1C). In our studies, TPO-Li was used due to the high absorption coefficient around 405 nm. We optimized the concentration of TPO-Li to be at 2% v/v for our hydrogel printing. We arbitrarily chose three ratios of the monomer to crosslinker, namely, 10% acrylamide: 0.15% bis-acrylamide, 10% acrylamide: 0.30% bis-acrylamide, and 10% acrylamide: 1.2% bis-acrylamide. The use of increasing crosslinker concentrations was intended to result in different stiffnesses ranging from soft to stiff[26] and varying microstructures.

To measure the stiffness of these PAA substrates, we used the SAOS rheology technique. All samples were viscoelastic with the storage modulus G' greater than the loss modulus G'' ($\tan \delta < 1$). Increasing the amount of crosslinker significantly affected network formation and substrate stiffness (Figure 1D,E). As displayed in Figure 1D, the storage modulus for the 1.2% bis-acrylamide substrate at low frequency was G' = 15,000 ± 100 Pa. This was four times higher than the 0.30% bis-acrylamide (G' = 3700 ± 100 Pa) and seventeen times higher than the 0.15% bis-acrylamide (G' = 855 ± 20 Pa). The greater stiffness of the 1.2% bis-acrylamide was also evidenced by it being the only sample for which G' was completely independent of frequency. The loss moduli G'' also decreased with decreasing ratio of bis-acrylamide from 575 ± 6 Pa (1.2% bis-acrylamide) to 78 ± 1 Pa (0.15% bis-acrylamide). Based on these results, the substrates are hereafter referred to as soft (0.15% bis bis-acrylamide), intermediate (0.30% bis-acrylamide), and stiff (1.2% bis-acrylamide).

3.2. Swelling Ratio of Different PAA Substrates Predicts Differential Pore Stretchability. To determine the physical properties of the printed PAA substrates, we evaluated the swelling ratio and saturation time of the soft, intermediate, and stiff substrates. The saturation time of a gel is the time required to reach its saturation state when no further

https://doi.org/10.1021/acsomega.2c01817
ACS Omega 2022, 7, 24384−24395

swelling can take place. The swelling ratio of soft, intermediate, and stiff gels from the dehydrated state (by alcohol dehydration) to the saturated state at different time intervals is plotted in Figure 2A. Figure 2A shows that the swelling ratio was very rapid in the initial stages but gradually diminishes until it reaches the saturation point. Figure 2A also displays different swelling ratios for different acrylamide to bis-acrylamide concentrations. The swelling ratio at the saturation point of the soft gel was found to be ∼900% while the intermediate and stiff gels exhibited a swelling ratio at saturation of ∼675% and ∼350%, respectively. Next, we evaluated the saturation time of the soft, intermediate, and stiff gels. The intersection of the initial slope of swelling and the slope of the saturation line provides us with the saturation time. In Figure 2B, we observe that the soft gel requires ∼35 min to reach saturation while the intermediate and stiff gels require ∼28 min and ∼15 min, respectively. From these two figures (Figure 2A,B), we show that the soft gel matrix is more stretchable than the stiff and intermediate gels.

Next, we ask the question, what would be the source of stretchability? Why would the soft gels swell up to 900% compared to the stiff gel swelling up to 350%? To address this question, we studied the microstructure of pores of the dehydrated soft, intermediate, and stiff gels with SEM. Although the SEM images are not representative of actual hydrated states, they can show a relative comparison of pores for different gels (Figure 3A−C).[27] It can be observed that both soft and intermediate gels have relatively similar large pore sizes, while the stiff gel showed very small pore sizes. In Figure 3D,E, we quantified the area and circularity of pores for soft, intermediate, and stiff gels. The average pore area of soft and intermediate gels was between 9000 and 11,000 μm^2 (Figure 3D). In comparison, the stiff gel pore area was ∼1000 μm^2 (Figure 3D). We computed the circularity index[28] or cell shape index ($CSI = \frac{4 \bullet \pi \bullet Area}{Perimeter^2}$) of each pore for soft, intermediate, and stiff gels, which indicates the roundness of each pore. For a perfect circle, the CSI is 1.0. The mean CSI of pores for soft, intermediate, and stiff gels were between 0.6 and 0.8 indicating moderate roundness (Figure 3E).

Interestingly, the thickness of the pores progressively increased from soft to stiff gels (Figure 3F). A box-whisker plot in Figure 3F shows the distribution of boundary thickness of the pores of soft, intermediate, and stiff gels with mean thicknesses of ∼5, 10, and 15 μm, respectively. Due to the largest pore area size and smallest thickness of 5 μm, the pores of the soft gels can be viewed to be loosely attached to each other. In other words, they can be easily stretched. For this very reason, during the swelling experiment, the liquid was allowed to permeate, stretch, and deform each pore, and swelled up to a massive 900% compared to its dehydrated state. In soft gels, the meshes were loosely attached to each other. Therefore, when water sipped into the pores, it stretched the pore size by applying pressure on the pore wall or matrix. That extra space allowed more water to sip in to fill up the space and it continued until the meshes had stretched up to their maximum, at this point the gels are at their saturation state. At this state, the gels swell to their maximum volume and stay constant without changing the volume.[29] In contrast, the pores were strong in intermediate gels and much stronger for stiff gels compared to soft gels. Much of the volume of the stiff gels was occupied by the thick boundaries and allowed less liquid to be retained during the swelling experiments inside its three-dimensional matrix.

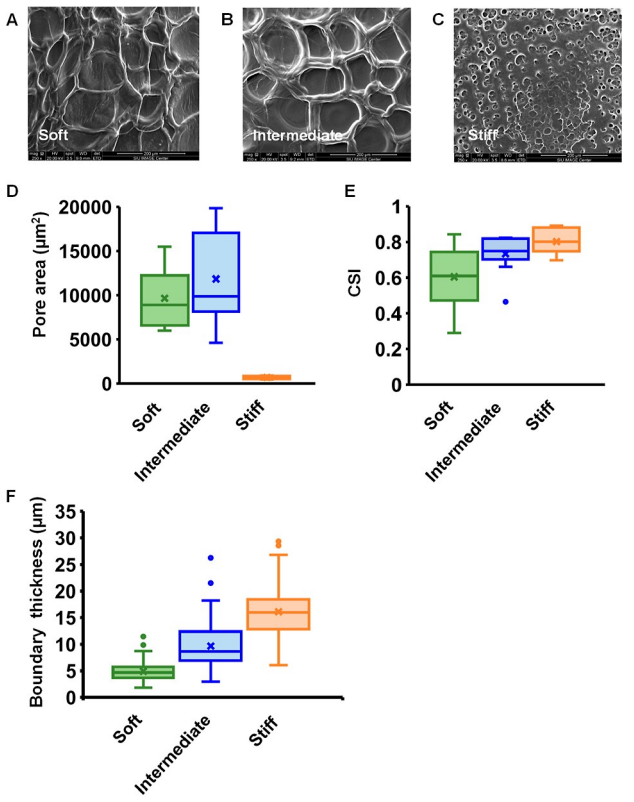

Figure 3. Pore size comparison of additively manufactured PAA substrates by SEM studies. (A−C) SEM images of additively manufactured PAA substrates show varying pore sizes. The pore size was highest for the soft gel while the lowest for the stiff gels. The pore size of intermediate gels was found to be similar to the soft gels. (D) Pore area quantification of soft, intermediate, and stiff substrates. A box-whisker plot shows the distribution of pores size for each substrate. (E) Box-whisker plot showing the circularity index or CSI of each pore for soft, intermediate, and stiff substrates. (F) Box-whisker plot showing the distribution of the boundary thickness. As the stiffness increased, the pore thickness increased concomitantly.

3.3. Homogeneous and Uniform Bead Distribution of Fluorescent Fiducial Markers is Achieved by Additive Manufacturing. Flexible PAA substrates are widely used in cell mechanosensing studies including TFM. During conventional manufacturing of PAA substrates, fiducial markers such as fluorescent microbeads (e.g., FITC-tagged microbeads) are generally added to the monomer and crosslinker mixture to observe and quantify the displacement field.[30] During the polymerization process, the microbeads are distributed randomly throughout the gel matrix.[31,32] Here, we compared the bead distribution in additively manufactured and conventionally prepared gels (Figure 4). After qualitative examination of Figure 4A,C, it is quite evident that the bead distribution of additively manufactured gels is far superior to the conventionally prepared gels. Having a uniform and homogeneous distribution will be very attractive and beneficial for single live-cell analysis.[33] We will test this feature of additively manufactured gels in the later part of the study.

To perform a quantitative analysis of bead distribution, images were acquired under the microscope and the presence of microbeads was detected by the FITC signal. The acquired images (Figure 4A,C) were divided into four quadrants, Q1−

https://doi.org/10.1021/acsomega.2c01817
ACS Omega 2022, 7, 24384−24395

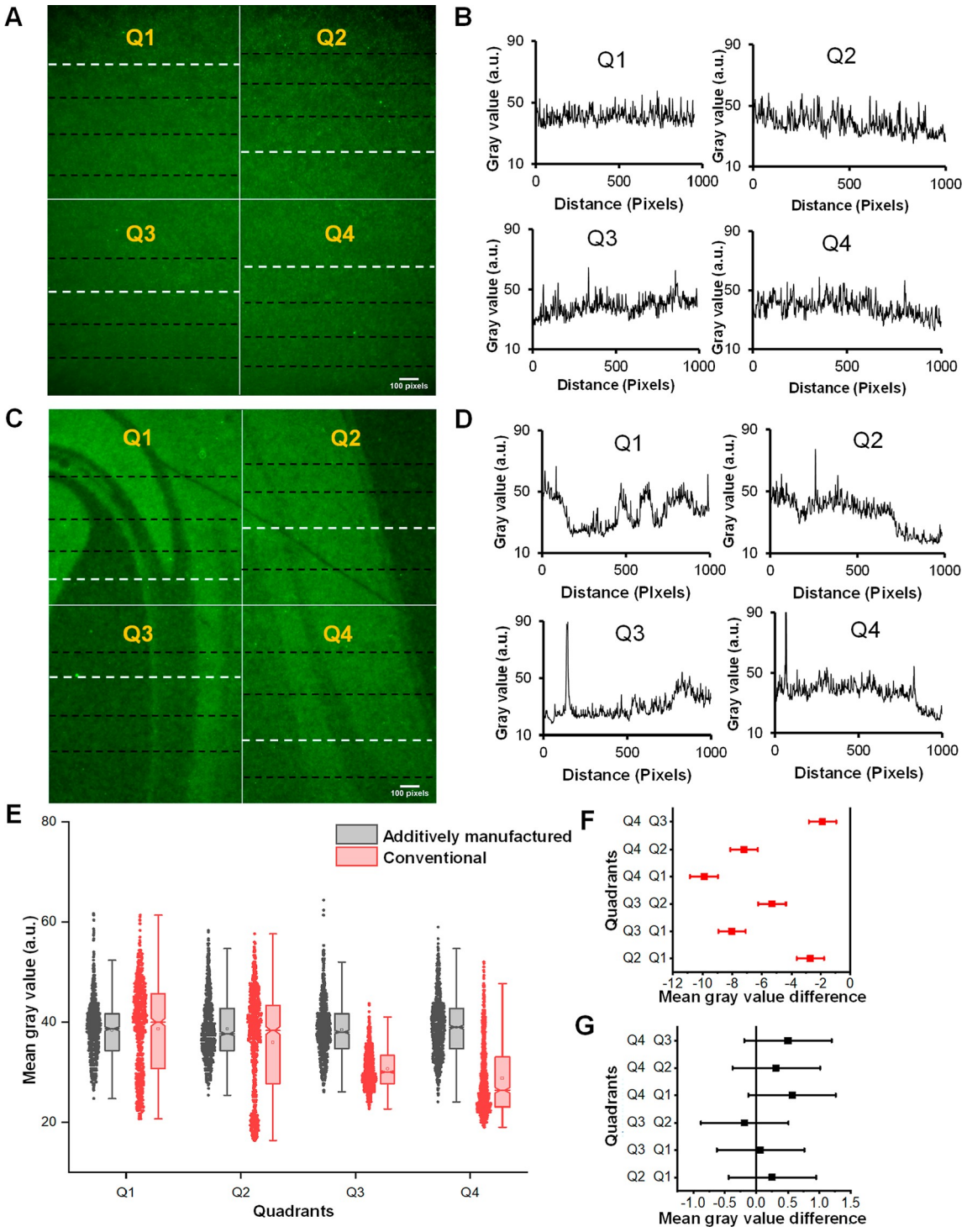

Figure 4. Embedded microbead distribution analysis of additively manufactured and conventionally made PAA substrates. (A,B) Fluorescence image of an additively manufactured PAA substrate. The embedded microbead labeled with FITC serves as a fiducial marker. The image was divided into four quadrants (Q1, Q2, Q3, and Q4), and four arbitrary lines were drawn on each quadrant. A line plot of representative lines (white) from each quadrant of the additively manufactured substrate is presented here. Gray value distribution remained similar for all four lines suggesting that there is a homogenous composition. The presence of microbeads tagged with FITC gives rise to the peaks on the plot. (C,D) Fluorescence image of a conventionally prepared substrate is displayed here. As before, the image was divided into four quadrants (Q1−Q4) and four arbitrary lines were drawn on each quadrant. Streaks and clusters of microbeads can be observed throughout the image resulting in a heterogeneous composition. The gray value of a representative line (white) from each quadrant of conventionally prepared substrate shows a large variation in bead distribution. (E) Mean gray value distribution in all four quadrants of additively manufactured (gray) and conventionally made (red) substrates are shown. Mean gray value calculation is performed from four representative lines of each quadrant. (F) Relative comparison between each quadrant of the conventional substrate is shown. A large variation in the mean gray value indicates a significant difference in each quadrant. For a homogeneous distribution, the difference should be close to zero; $p < 0.05$. (G) Relative comparison between each quadrant of additively manufactured substrates showing slight variation in mean value, suggesting a homogeneous distribution; $p > 0.05$.

https://doi.org/10.1021/acsomega.2c01817
ACS Omega 2022, 7, 24384−24395

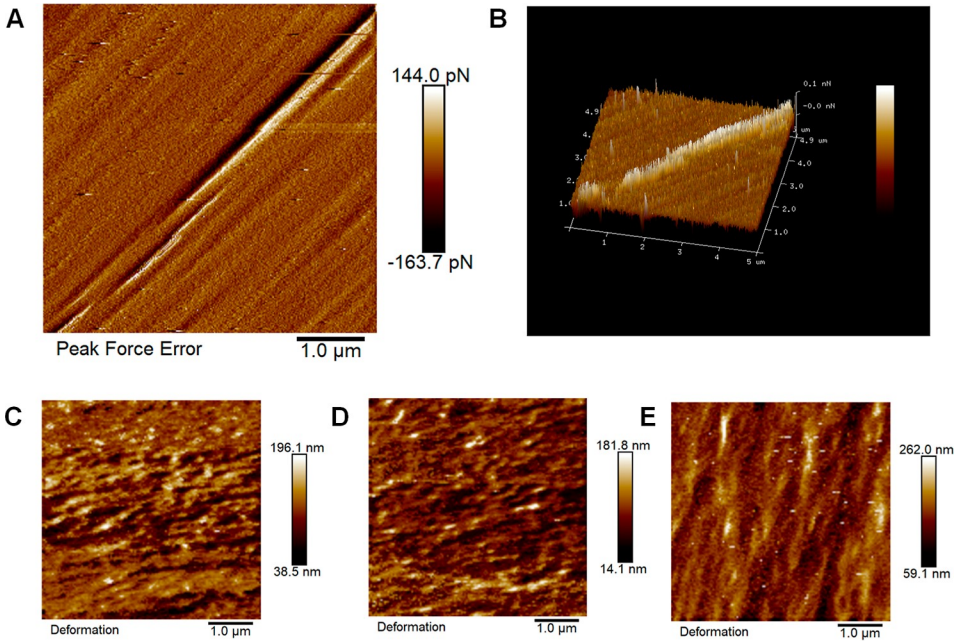

Figure 5. Surface feature analysis of additively manufactured PAA substrates by atomic force microscopy. (A) Peak force quantitative nanomechanical mapping (PFQNM) of PAA substrates in 2D is displayed here. Visible surface features were mapped in peak force error. Surface anomalies and features are visible at this scale. (B) Peak force distribution in 3D format. High-resolution descriptive image showing ridge and crevices formation along the plane. (C–E) Deformation maps of soft (c), intermediate (d), and stiff (e) substrates are shown here.

Q4. Representative four lines were drawn arbitrarily on each quadrant. By analyzing the gray value of each pixel along the lines using the ImageJ software, we plotted the graphs (Figure 4B,D). The line plot shown in Figure 4B,D represents the white lines shown in Figure 4A,C respectively. By comparing the representative lines (Figure 4B,D), we could readily see that the conventionally prepared gels exhibit random peaks and troughs (Figure 4D) which arise from uncontrolled bead distribution resulting in streaks and clusters as shown in Figure 4C. In contrast, in the additively manufactured gels (Figure 4A), the bead distribution was uniform throughout the gel matrix and there were no clusters, streaks, or dark patches present. As a result, the line plots in Figure 4B show consistent flat lines with peaks (presence of microbead) and troughs (absence of microbead) appearing in regular intervals.

For a thorough statistical analysis of the microbead distribution throughout the quadrants, we plotted a box-whisker plot of the mean gray value of the pixels from the line plots as shown in Figure 4E. The mean gray value of the randomly selected lines (black) from each quadrant were combined together, which displays almost identical distribution in all four quadrants for additively manufactured gels. However, the microbead distribution of conventional gels was highly spread and uneven among the quadrants. Clustering of microbeads in the four quadrants leads to significant variation. This became more evident with the mean gray value difference between the quadrants. When we plotted the difference in mean gray value in Figure 4F, we found that the mean gray value difference for conventional gels was far from zero, in all four quadrants. In the case of additively manufactured gels (Figure 4G), the mean gray value difference between each quadrant was very close to zero, with no statistically significant difference being observed (one-way ANOVA p-value >0.05 for additively manufactured gels). Ideally, the difference in mean gray value between quadrants should be zero or close to zero for uniform and homogenous distributions.

3.4. PAA Hydrogels Do Not Show Significant Changes in Surface Roughness that may Affect Living Cell Functions. Surface topography, such as surface roughness, can be crucial for living cell applications.[34,35] To evaluate the surface topology of additively manufactured PAA substrates, we used AFM. Additively manufactured PAA substrates were immersed in water before running assays with AFM to mimic the natural state of the gels. Surface roughness was analyzed in NanoScope Analysis which measured the roughness parameters.[36] Surface parameters obtained were R_q (root mean square deviation), R_a (arithmetic mean deviation), R_{sk} (skewness), and R_{ku} (kurtosis).[37] Data was obtained by analyzing a 5 μm × 5 μm area from the surface of each gel type. Both the rms surface roughness, R_q, and arithmetic surface roughness, R_a, values of the gels were quite similar, within the range of ∼ 20–25 nm (Figure 5; Table 2). This implied that regardless of the different concentrations of gels, the surface features, that is, peaks and crevices were not significantly different than each other. The values for R_{sk} or skewness also showed close to range (0.118, 0.578, and 1.54) positive values, which meant the deviation was beneath the mean distribution line and the surfaces mainly featured peaks and asperities. The surface peak profile was sharp for all three gels showing an R_{ku} > 3 with an uneven height distribution. From the table, we could say that the surface features observed in different types of gels varied little and will not have a significant impact on living cell studies due to their size

Table 2. Common Surface Roughness Parameters for Additively Manufactured PAA Substrates

hydrogel type	R_q (nm)	R_a (nm)	R_{sk}	R_{ku}
soft	22.9	18.2	0.118	3.57
intermediate	23.8	18.7	0.578	4.85
stiff	25.4	18.2	1.54	10.8

https://doi.org/10.1021/acsomega.2c01817
ACS Omega 2022, 7, 24384–24395

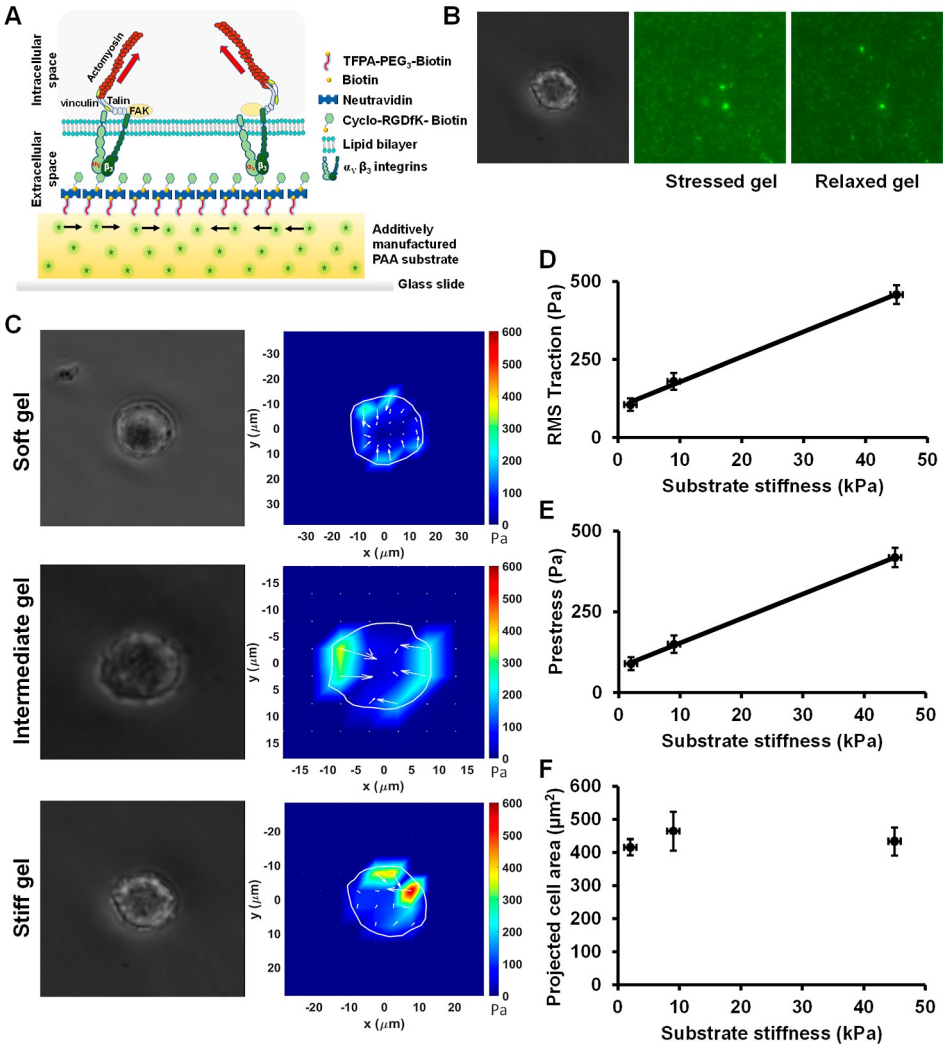

Figure 6. TFM analysis of B16F1 mouse melanoma cells on additively manufactured PAA substrates of varying stiffness. (A) Schematic illustration of RGDfK peptide conjugation on an additively manufactured PAA substrate. (B) FITC-conjugated microbead distribution on the PAA substrate surface is presented here before (stressed) and after (relaxed) cell trypsinization. The relative displacement of microbeads can be readily observed before and after trypsinization images. (C) Phase and traction maps of B16F1 cells on additively manufactured PAA substrates of varying stiffnesses are displayed here. The top, middle, and bottom rows show the soft, intermediate, and stiff gel responses, respectively. (D) rms traction of B16F1 cells on different stiffness gels shows that with increasing gel stiffness, rms traction increases linearly. $n = 12$, data represents mean ± s.e. $R^2 \approx 1.0$. (E) Concomitant increase in cell prestress is also observed with increasing gel stiffness. $n = 12$, data represents mean ± s.e. $R^2 \approx 1.0$. (F) Very similar cell spreading is observed across all substrate rigidity; $p > 0.05$, $n = 12$, data represents mean ± s.e.

difference. For perspective, living cell sizes, such as B16F1, MEF, and HeLa cells, range from at least 10 to 20 μm or greater[38−40] whereas the surface features of gels were in nm scale. Comparing the scale size of the cell and the similarity in gel surface roughness among different stiffness, we expect the impact of the gel surface roughness feature on live-cell measurements would be negligible. Data were also obtained for conventionally made PAA gels as a control, which showed similar features as additively manufactured gels (Supporting Information Table S1 and Figure S1).

3.5. Viscoelastic PAA Substrates Reveal a Novel Mechanosensing Feature. The PAA substrates are very attractive to the mechanobiology research community because of the ability to tune the mechanical stiffness via adjusting the ratio of acrylamide monomer and bis-acrylamide crosslinker content.[41] In addition, the crosslinked PAA substrates are biologically inert, making them suitable for cell substrates with a variety of functionalization opportunities.[42] Furthermore, we demonstrated in Figure 4 that the additively manufactured gel composition is homogeneous, as measured by the bead distribution throughout the gel. Moreover, the additively manufactured PAA substrates show dissipative behavior mimicking living tissues. Altogether, we can investigate cell mechanosensing on additively manufactured PAA substrates of varying viscoelastic properties by interrogating basic cell traction response. It would provide us with more accurate, reliable, and physiologically relevant information.

A cartoon showing a cell segment locally adhered on top of the PAA substrate via integrins $\alpha_v\beta_3$ and exerting traction forces resulting in bead displacements (Figure 6A). Figure 6B displays actual bead displacement before and after cell attachment on the viscoelastic PAA substrate. The traction stress generated at the cell−substrate interface is balanced by internal cell prestress.[43,44] A representative traction image of B16F1 cells on soft, intermediate, and stiff gels is displayed in Figure 6C. As the stiffness of the substrates increases, the peak

https://doi.org/10.1021/acsomega.2c01817
ACS Omega 2022, 7, 24384−24395

stress, as well as the root mean square (rms) traction also increases. As expected, the traction stress generated around the cell boundary was more elevated than the central regions of the cell[25,43] possibly due to the location of the nucleus, where fewer focal adhesions would be formed. The rms traction and corresponding prestress values of single B16F1 cells on different viscoelastic PAA substrates are summarized in Figure 6D,E which shows a linear trend in traction and corresponding prestress increase as a function of increasing substrate stiffness. Best fitted lines were also plotted (Figure 6D,E), considering the rms traction and prestress relation to soft, intermediate, and stiff substrates. In Figure 6F, the projected cell area is shown for different substrate stiffnesses. Unexpectedly, cells did not spread in the early hours with increasing underlying substrate stiffness. This suggests cells are sensitive to viscous solids and cell shape can be decoupled from rms traction and cytoskeletal prestress. This is consistent with the data presented by Charrier et al., where 3T3 fibroblasts exhibited overall smaller areas on viscoelastic substrates compared to purely elastic substrates.[42] As a control experiment, when cells were seeded on 0.6 versus 8.5 kPa substrates, the projected cell area increased as a function of underlying substrate stiffness (Supporting Information Figure S2). Similarly, as the underlying substrate stiffness increased, cell traction also increased (Supporting Information Figure S2).

4. DISCUSSION

Conventionally made crosslinked PAA substrates are reported to behave as purely linearly elastic substrates.[42,45] Here, we report that additively manufactured PAA substrates behave as viscoelastic solids. This is a significant observation that has not been reported before. However, what would be the source of dissipation in the additively manufactured crosslinked PAA substrates? Most often, the polymer matrix exhibits viscous dissipation due to the internal friction of the whole polymer chain arising from the viscous/fluid chain motion in the network matrix. Previously, it has been demonstrated that entrapping viscous chains within an elastic crosslinked network can generate dissipative polymers.[42,46] We speculate that something similar has happened due to the inherent nature of SLA additive manufacturing. During additive manufacturing, each layer is exposed to the UV light source for a predetermined exposure time. After the elapsed exposure time of the first layer, the printing base is lifted by the amount of the layer height thickness and the printing of the second layer begins. At the beginning of printing the second layer, it may be very possible to have a semi-cured resin mix to be entrapped in the first layer. With consecutive layer deposition, the overall outcome would be the presence of semi-cured resin mixtures, representing the viscous fluid chains, entrapped and distributed uniformly throughout the gel. Because we did not perform any postcuring process, the cured: semi-cured resin mixture could contribute to the viscoelastic nature of the gel. This is also supported by the fact that the loss moduli of the gels decrease with increasing bis-acrylamide (crosslinker) content.

Living tissues exhibit a loss modulus between 10 and 20% of their elastic modulus.[42,47] Nevertheless, the majority of the mechanosensing studies relied on crosslinked PAA gels that are purely elastic and exhibit very little to no loss modulus over a wide range of time scales.[45] Our current understanding of how cells interpret physical and mechanical cues from physiologically relevant viscoelastic substrates (mimicking living tissue) remains poor. Unlike the conventionally made crosslinked PAA gels, additively manufactured PAA gels exhibited a decent 5−10% loss moduli relative to their elastic storage moduli. We established the basic relationships between cell traction, cytoskeletal prestress, and early cell spreading, which happens to be the first and foremost deciding factor in many mechanosensing events including stem cell differentiation, cancer progression, and immune response.[1] From our basic understanding of adherent contractile cells on crosslinked PAA gels, as the substrate moduli increase, cell spreading also increases with a concomitant increase in cell traction and cytoskeletal prestress.[22,43,11,48] In other words, early cell spreading, cell traction, and cytoskeletal prestress are coupled together and are tightly regulated, which was also evident from a micropatterned adhesive island study.[49] However, early cell spreading on our additively manufactured PAA substrates of different stiffness remained almost similar, but cells were able to increase traction and cytoskeletal prestress with increasing substrate moduli, indicating a decoupling of cell spreading from cell traction and cytoskeletal prestress. Consistent with our findings, fibroblast and human hepatocytes were also found to spread less with increasing viscoelastic properties of the substrates (although not with additively manufactured PAA viscoelastic substrates).[50] Along the line, a recent report showed limited cell spreading response on viscoelastic substrates,[51] possibly due to the Rho family of small GTPases activity.[52] In contrast, the cell spreading and proliferation in 3D alginate-based viscoelastic matrix demonstrates that cell spreading and proliferation increase with increasing viscoelasticity.[53] This apparently disparate outcome of cell spreading and proliferation with increasing viscoelasticity may be linked to the concept of 3D mechanical confinements.

Chan and Odde, in 2008, developed a computational molecular "motor-clutch" model to explain higher traction force generation with a spread area, where the compliant substrates were modeled as elastic springs.[54] In the future, to explain the decoupling of cell spreading and traction stress generation, we will develop a computational model that includes both springs and dashpots to represent our additively manufactured viscoelastic PAA substrates. Additionally, to mimic tissue moduli, various combinations of monomer, crosslinker, and UV light exposure time can be used to additively manufacture gels with varying loss moduli. One additional important parameter we have not addressed here is the stiffness of cells on our viscoelastic PAA substrates and how apical cell stiffness would be regulated with basal traction stresses. We intend to investigate this in the future.

Hydrogels are extensively studied for potential use in devices with specific applications in bioelectronics and soft machines including wearable devices, soft robotics, stretchable ionic devices, and energy harvesting devices.[55] The hydrogels are soft, biocompatible, and allow myriads of functionalization that permits a wide range of sensing capabilities. As a result, there is a significant thrust in developing skin-like hydrogels for wearable electronics.[55] In addition, PAA hydrogels are used extensively in the biomedical and biotechnology fields.[56,57] Our additively manufactured PAA gels have a homogenous microstructural composition with tunable porosity which will be an asset for western blots, DNA extraction and cleanup, gel electrophoresis, and purification columns. Moreover, our technique can be a strength for additive manufacturing of skin-like hydrogels for tissue engineering applications which remains to be explored in the future. Furthermore, soft

https://doi.org/10.1021/acsomega.2c01817
ACS Omega 2022, 7, 24384−24395

polymers with gel consistency are increasingly being used in the additive manufacture of batteries.[58] The three-dimensional polymer network that allows retaining a large volume of electrolytes can be very useful for battery design. In particular, the porosity of the separator is very crucial for the performance and safety of batteries. In our work, we have demonstrated a greater control of specific pore size and pore boundary thickness that can generally be utilized in novel battery designs.

5. CONCLUSIONS

Taken together, we demonstrate a novel method to create homogeneous and viscoelastic PAA hydrogels, that mimics real tissues, to show that single living cells are very sensitive to the dissipative component of the hydrogels. Decoupling cell spreading from traction and cytoskeletal prestress is a novel finding which has not been reported in studies conducted on purely elastic PAA substrates. Furthermore, the fabrication of PAA substrates can become a bottleneck and may cause reproducibility issues due to the inherent limitations of the conventional fabrication process including the lengthy step-wise protocol, less control of local properties, and dependence on the user expertise level. The vat photopolymerization technique allowed us to manufacture PAA substrates with tunable viscoelastic properties and homogeneous structural composition and eliminate the shortcomings of conventional manufacturing altogether. Future studies will be aimed at independently controlling the dissipative nature of the PAA substrates.

■ ASSOCIATED CONTENT

Supporting Information

The Supporting Information is available free of charge at https://pubs.acs.org/doi/10.1021/acsomega.2c01817.

Common surface roughness parameters for conventionally made PAA substrates, PFQNM of conventionally made substrates in 2D, and projected cell area and cell traction as a function of substrate (conventionally made) stiffness (PDF)

■ AUTHOR INFORMATION

Corresponding Authors

Virginia A. Davis − *Samuel Ginn Department of Chemical Engineering, Auburn University, Auburn, Alabama 36849, United States;* orcid.org/0000-0003-3126-3893; Email: davisva@auburn.edu

Sabrina Nilufar − *School of Mechanical, Aerospace, and Materials Engineering, Southern Illinois University Carbondale, Carbondale, Illinois 62901, United States;* Email: sabrina.nilufar@siu.edu

Farhan Chowdhury − *School of Mechanical, Aerospace, and Materials Engineering, Southern Illinois University Carbondale, Carbondale, Illinois 62901, United States; Biomedical Engineering Program, School of Electrical, Computer, and Biomedical Engineering and Materials Technology Center, Southern Illinois University Carbondale, Carbondale, Illinois 62901, United States;* orcid.org/0000-0003-1527-2677; Email: farhan.chowdhury@siu.edu

Authors

Fardeen Kabir Protick − *School of Mechanical, Aerospace, and Materials Engineering, Southern Illinois University Carbondale, Carbondale, Illinois 62901, United States*

Sadat Kamal Amit − *Samuel Ginn Department of Chemical Engineering, Auburn University, Auburn, Alabama 36849, United States;* orcid.org/0000-0001-7057-0971

Kshitij Amar − *School of Mechanical, Aerospace, and Materials Engineering, Southern Illinois University Carbondale, Carbondale, Illinois 62901, United States;* Present Address: Department of Mechanical Science and Engineering, the University of Illinois at Urbana-Champaign, Urbana, IL 61801, United States

Shukantu Dev Nath − *School of Mechanical, Aerospace, and Materials Engineering, Southern Illinois University Carbondale, Carbondale, Illinois 62901, United States*

Rafee Akand − *School of Mechanical, Aerospace, and Materials Engineering, Southern Illinois University Carbondale, Carbondale, Illinois 62901, United States*

Complete contact information is available at: https://pubs.acs.org/10.1021/acsomega.2c01817

Author Contributions

S.K.A., K.A., and S.D.N. contributed equally. F.C and S.N. conceived the project. F.C., S.N., and V.A.D. designed the experiments. F.K.P., S.K.A, S.D.N, and K.A. performed the experiments and/or analyzed/summarized the data. All authors discussed the results and wrote the manuscript.

Notes

The authors declare no competing financial interest.

■ ACKNOWLEDGMENTS

F.C. acknowledges the support of NIH grant GM148440 and NSF CHE 1920255. The work was partly supported by Elsa U. Pardee Foundation (F.C.). S.N. would like to acknowledge the NSF grant (award #: 2138459). Additionally, F.C. and S.N. thank NSF DMR and DoD Assure REU program (award #: 1757954) and Materials Technology Center at SIUC. We thank Sakib Mohammad and Fayed Alshammari for their technical assistance.

■ REFERENCES

(1) Chowdhury, F.; Huang, B.; Wang, N. Cytoskeletal prestress: The cellular hallmark in mechanobiology and mechanomedicine. *Cytoskeleton* **2021**, *78*, 249−276.

(2) Petrie, R. J.; Yamada, K. M. At the leading edge of three-dimensional cell migration. *J. Cell Sci.* **2012**, *125*, 5917.

(3) Espina, J. A.; Marchant, C. L.; Barriga, E. H. Durotaxis: the mechanical control of directed cell migration. *FEBS J.* **2022**, *289*, 2736.

(4) Shin, M. E.; He, Y.; Li, D.; Na, S.; Chowdhury, F.; Poh, Y.-C.; Collin, O.; Su, P.; de Lanerolle, P.; Schwartz, M. A.; Wang, N.; Wang, F. Spatiotemporal organization, regulation, and functions of tractions during neutrophil chemotaxis. *Blood* **2010**, *116*, 3297−3310.

(5) Kumar, A.; Placone, J. K.; Engler, A. J. Understanding the extracellular forces that determine cell fate and maintenance. *Development* **2017**, *144*, 4261−4270.

(6) Discher, D. E.; Mooney, D. J.; Zandstra, P. W. Growth factors, matrices, and forces combine and control stem cells. *Science* **2009**, *324*, 1673−1677.

(7) Li, D.; Zhou, J.; Chowdhury, F.; Cheng, J.; Wang, N.; Wang, F. Role of mechanical factors in fate decisions of stem cells. *Regen. Med.* **2011**, *6*, 229−240.

(8) Blumenthal, D.; Burkhardt, J. K. Multiple actin networks coordinate mechanotransduction at the immunological synapse. *J. Cell Biol.* **2020**, *219*, No. e201911058.

(9) Broders-Bondon, F.; Nguyen Ho-Bouldoires, T. H.; Fernandez-Sanchez, M.-E.; Farge, E. Mechanotransduction in tumor progression: The dark side of the force. *J. Cell Biol.* **2018**, *217*, 1571−1587.
(10) Kumar, S. Stiffness does matter. *Nat. Mater.* **2014**, *13*, 918−920.
(11) Solon, J.; Levental, I.; Sengupta, K.; Georges, P. C.; Janmey, P. A. Fibroblast Adaptation and Stiffness Matching to Soft Elastic Substrates. *Biophys. J.* **2007**, *93*, 4453−4461.
(12) Tajik, A.; Zhang, Y.; Wei, F.; Sun, J.; Jia, Q.; Zhou, W.; Singh, R.; Khanna, N.; Belmont, A. S.; Wang, N. Transcription upregulation via force-induced direct stretching of chromatin. *Nat. Mater.* **2016**, *15*, 1287−1296.
(13) Guilluy, C.; Burridge, K. Nuclear mechanotransduction: Forcing the nucleus to respond. *Nucleus* **2015**, *6*, 19−22.
(14) Uhler, C.; Shivashankar, G. V. Regulation of genome organization and gene expression by nuclear mechanotransduction. *Nat. Rev. Mol. Cell Biol.* **2017**, *18*, 717−727.
(15) Nath, S. D.; Nilufar, S. An Overview of Additive Manufacturing of Polymers and Associated Composites. *Polymers* **2020**, *12*, 2719.
(16) Williams, C. G.; Malik, A. N.; Kim, T. K.; Manson, P. N.; Elisseeff, J. H. Variable cytocompatibility of six cell lines with photoinitiators used for polymerizing hydrogels and cell encapsulation. *Biomaterials* **2005**, *26*, 1211−1218.
(17) Pawar, A. A.; Saada, G.; Cooperstein, I.; Larush, L.; Jackman, J. A.; Tabaei, S. R.; Cho, N. J.; Magdassi, S. High-performance 3D printing of hydrogels by water-dispersible photoinitiator nanoparticles. *Sci. Adv.* **2016**, *2*, No. e1501381.
(18) Wang, J.; Stanic, S.; Altun, A. A.; Schwentenwein, M.; Dietliker, K.; Jin, L.; Stampfl, J.; Baudis, S.; Liska, R.; Grützmacher, H. A highly efficient waterborne photoinitiator for visible-light-induced three-dimensional printing of hydrogels. *Chem. Commun.* **2018**, *54*, 920−923.
(19) Fairbanks, B. D.; Schwartz, M. P.; Bowman, C. N.; Anseth, K. S. Photoinitiated polymerization of PEG-diacrylate with lithium phenyl-2,4,6-trimethylbenzoylphosphinate: polymerization rate and cytocompatibility. *Biomaterials* **2009**, *30*, 6702−6707.
(20) Markovic, M.; Van Hoorick, J.; Hölzl, K.; Tromayer, M.; Gruber, P.; Nürnberger, S.; Dubruel, P.; Van Vlierberghe, S.; Liska, R.; Ovsianikov, A. Hybrid Tissue Engineering Scaffolds by Combination of Three-Dimensional Printing and Cell Photoencapsulation. *J. Nanotechnol. Eng. Med.* **2015**, *6*, 0210011−210017.
(21) Dembo, M.; Wang, Y.-L. Stresses at the cell-to-substrate interface during locomotion of fibroblasts. *Biophys. J.* **1999**, *76*, 2307−2316.
(22) Pelham, R. J.; Wang, Y.-l. Cell locomotion and focal adhesions are regulated by substrate flexibility. *Proc. Natl. Acad. Sci. U.S.A.* **1997**, *94*, 13661−13665.
(23) Yeung, T.; Georges, P. C.; Flanagan, L. A.; Marg, B.; Ortiz, M.; Funaki, M.; Zahir, N.; Ming, W.; Weaver, V.; Janmey, P. A. Effects of substrate stiffness on cell morphology, cytoskeletal structure, and adhesion. *Cell Motil.* **2005**, *60*, 24−34.
(24) Engler, A.; Bacakova, L.; Newman, C.; Hategan, A.; Griffin, M.; Discher, D. Substrate Compliance versus Ligand Density in Cell on Gel Responses. *Biophys. J.* **2004**, *86*, 617−628.
(25) Butler, J. P.; Tolić-Nørrelykke, I. M.; Fabry, B.; Fredberg, J. J. Traction fields, moments, and strain energy that cells exert on their surroundings. *Am. J. Physiol.: Cell Physiol.* **2002**, *282*, C595−C605.
(26) Tse, J. R.; Engler, A. J. Preparation of hydrogel substrates with tunable mechanical properties. *Curr. Protoc. Cell Biol.* **2010**, *10*, 10.16.
(27) Wen, J. H.; Vincent, L. G.; Fuhrmann, A.; Choi, Y. S.; Hribar, K. C.; Taylor-Weiner, H.; Chen, S.; Engler, A. J. Interplay of matrix stiffness and protein tethering in stem cell differentiation. *Nat. Mater.* **2014**, *13*, 979−987.
(28) Chowdhury, F.; Li, I. T. S.; Leslie, B. J.; Doğanay, S.; Singh, R.; Wang, X.; Seong, J.; Lee, S.-H.; Park, S.; Wang, N.; Ha, T. Single molecular force across single integrins dictates cell spreading. *Integr. Biol.* **2015**, *7*, 1265−1271.
(29) Mabilleau, G.; Baslé, M. F.; Chappard, D. Evaluation of Surface Roughness of Hydrogels by Fractal Texture Analysis during Swelling. *Langmuir* **2006**, *22*, 4843−4845.
(30) Muhamed, I.; Chowdhury, F.; Maruthamuthu, V. Biophysical Tools to Study Cellular Mechanotransduction. *Bioengineering* **2017**, *4*, 12.
(31) Bestvater, F.; Spiess, E.; Stobrawa, G.; Hacker, M.; Feurer, T.; Porwol, T.; Berchner-Pfannschmidt, U.; Wotzlaw, C.; Acker, H. Two-photon fluorescence absorption and emission spectra of dyes relevant for cell imaging. *J. Microsc.* **2002**, *208*, 108.
(32) Chowdhury, F.; Li, Y.; Poh, Y.-C.; Yokohama-Tamaki, T.; Wang, N.; Tanaka, T. S. Soft Substrates Promote Homogeneous Self-Renewal of Embryonic Stem Cells via Downregulating Cell-Matrix Tractions. *PLoS One* **2010**, *5*, No. e15655.
(33) Dembo, M.; Oliver, T.; Ishihara, A.; Jacobson, K. Imaging the traction stresses exerted by locomoting cells with the elastic substratum method. *Biophys. J.* **1996**, *70*, 2008−2022.
(34) Hou, Y.; Yu, L.; Xie, W.; Camacho, L. C.; Zhang, M.; Chu, Z.; Wei, Q.; Haag, R. Surface Roughness and Substrate Stiffness Synergize To Drive Cellular Mechanoresponse. *Nano Lett.* **2020**, *20*, 748−757.
(35) Dalby, M. J.; Gadegaard, N.; Oreffo, R. O. C. Harnessing nanotopography and integrin−matrix interactions to influence stem cell fate. *Nat. Mater.* **2014**, *13*, 558−569.
(36) Chinga, G.; Johnsen, P. O.; Dougherty, R.; Berli, E. L.; Walter, J. Quantification of the 3D microstructure of SC surfaces. *J. Microsc.* **2007**, *227*, 254−265.
(37) Balderrama, Í. d. F.; Stuani, V. d. T.; Cardoso, M. V.; Oliveira, R. C.; Lopes, M. M. R.; Greghi, S. L. A.; Adriana Campos Passanezi, S. A. The influence of implant surface roughness on decontamination by antimicrobial photodynamic therapy and chemical agents: A preliminary study in vitro. *Photodiagn. Photodyn. Ther.* **2021**, *33*, 102105.
(38) Nakamura, M.; Ono, D.; Sugita, S. Mechanophenotyping of B16 Melanoma Cell Variants for the Assessment of the Efficacy of (-)-Epigallocatechin Gallate Treatment Using a Tapered Microfluidic Device. *Micromachines* **2019**, *10*, 207.
(39) Turgay, Y.; Eibauer, M.; Goldman, A. E.; Shimi, T.; Khayat, M.; Ben-Harush, K.; Dubrovsky-Gaupp, A.; Sapra, K. T.; Goldman, R. D.; Medalia, O. The molecular architecture of lamins in somatic cells. *Nature* **2017**, *543*, 261−264.
(40) Borle, A. B. Kinetic analyses of calcium movements in HeLa cell cultures. I. Calcium influx. *J. Gen. Physiol.* **1969**, *53*, 43−56.
(41) Denisin, A. K.; Pruitt, B. L. Tuning the Range of Polyacrylamide Gel Stiffness for Mechanobiology Applications. *ACS Appl. Mater. Interfaces* **2016**, *8*, 21893−21902.
(42) Charrier, E. E.; Pogoda, K.; Wells, R. G.; Janmey, P. A. Control of cell morphology and differentiation by substrates with independently tunable elasticity and viscous dissipation. *Nat. Commun.* **2018**, *9*, 449.
(43) Wang, N.; Tolić-Nørrelykke, I. M.; Chen, J.; Mijailovich, S. M.; Butler, J. P.; Fredberg, J. J.; Stamenović, D. Cell prestress. I. Stiffness and prestress are closely associated in adherent contractile cells. *Am. J. Physiol.: Cell Physiol.* **2002**, *282*, C606−C616.
(44) Kulkarni, A. H.; Ghosh, P.; Seetharaman, A.; Kondaiah, P.; Gundiah, N. Traction cytometry: regularization in the Fourier approach and comparisons with finite element method. *Soft Matter* **2018**, *14*, 4687−4695.
(45) Chen, D. T. N.; Wen, Q.; Janmey, P. A.; Crocker, J. C.; Yodh, A. G. Rheology of Soft Materials. *Annu. Rev. Condens. Matter Phys.* **2010**, *1*, 301−322.
(46) Huang, J.; Xu, Y.; Qi, S.; Zhou, J.; Shi, W.; Zhao, T.; Liu, M. Ultrahigh energy-dissipation elastomers by precisely tailoring the relaxation of confined polymer fluids. *Nat. Commun.* **2021**, *12*, 3610.
(47) Elosegui-Artola, A. The extracellular matrix viscoelasticity as a regulator of cell and tissue dynamics. *Curr. Opin. Cell Biol.* **2021**, *72*, 10−18.

https://doi.org/10.1021/acsomega.2c01817
ACS Omega 2022, 7, 24384−24395

(48) Reinhart-King, C. A.; Dembo, M.; Hammer, D. A. The Dynamics and Mechanics of Endothelial Cell Spreading. *Biophys. J.* **2005**, *89*, 676−689.
(49) Wang, N.; Ostuni, E.; Whitesides, G. M.; Ingber, D. E. Micropatterning tractional forces in living cells. *Cell Motil. Cytoskelet.* **2002**, *52*, 97−106.
(50) Chaudhuri, O.; Cooper-White, J.; Janmey, P. A.; Mooney, D. J.; Shenoy, V. B. Effects of extracellular matrix viscoelasticity on cellular behaviour. *Nature* **2020**, *584*, 535−546.
(51) Charrier, E. E.; Pogoda, K.; Li, R.; Park, C. Y.; Fredberg, J. J.; Janmey, P. A. A novel method to make viscoelastic polyacrylamide gels for cell culture and traction force microscopy. *APL Bioeng.* **2020**, *4*, 036104.
(52) Chester, D.; Kathard, R.; Nortey, J.; Nellenbach, K.; Brown, A. C. Viscoelastic properties of microgel thin films control fibroblast modes of migration and pro-fibrotic responses. *Biomaterials* **2018**, *185*, 371−382.
(53) Chaudhuri, O.; Gu, L.; Klumpers, D.; Darnell, M.; Bencherif, S. A.; Weaver, J. C.; Huebsch, N.; Lee, H.-p.; Lippens, E.; Duda, G. N.; Mooney, D. J. Hydrogels with tunable stress relaxation regulate stem cell fate and activity. *Nat. Mater.* **2015**, *15*, 326−334.
(54) Chan, C. E.; Odde, D. J. Traction Dynamics of Filopodia on Compliant Substrates. *Science* **2008**, *322*, 1687−1691.
(55) Ying, B.; Liu, X. Skin-like hydrogel devices for wearable sensing, soft robotics and beyond. *iScience* **2021**, *24*, 103174.
(56) Magnusson, A. O.; Szekrenyi, A.; Joosten, H. J.; Finnigan, J.; Charnock, S.; Fessner, W. D. nanoDSF as screening tool for enzyme libraries and biotechnology development. *FEBS J.* **2018**, *286*, 184−204.
(57) Kumar, G. Principle and Method of Silver Staining of Proteins Separated by Sodium Dodecyl Sulfate−Polyacrylamide Gel Electrophoresis. In *Protein Gel Detection and Imaging*; Springer, 2018; pp 231−236.
(58) Wang, J.; Lu, T.; Yang, M.; Sun, D.; Xia, Y.; Wang, T. Hydrogel 3D printing with the capacitor edge effect. *Sci. Adv.* **2019**, *5*, No. eaau8769.

https://doi.org/10.1021/acsomega.2c01817
ACS Omega 2022, 7, 24384−24395